In-Depth Design and Multiobjective Optimization of an Integrated Transformer for Five-Phase LLC Resonant Converters

Jianing Wang, *Member, IEEE*, Jiawen Hu, Wei Pei, Zhiqing Yang, *Member, IEEE*, Jiacai Zhuang, and Xing Zhang, *Senior Member, IEEE*

***Abstract*—High-power isolated dc–dc converters are preferred in the medium-voltage cascaded H-bridge (CHB) photovoltaic (PV) generation systems due to high power density and galvanic isolation. However, high-power transformers in dc–dc converters can result in high power losses and poor heat dissipation due to thick isolation materials. The three-phase LLC (3P-LLC) converter has been reported suitable for high power applications. Comparing to the single-phase counterpart, the 3P-LLC converter employs three discrete transformers, leading to a larger core area for better heat dissipation. To further increase the power density and the heat dissipation capability of resonant converters, increasing the phase number and integrating magnetic components are considered. This work proposes a five-phase LLC (5P-LLC) resonant converter for the CHB PV application. To increase the power density, a five-phase magnetic integrated transformer (5P-MIT) is proposed and designed with an optimal limb structure to avoid local flux saturation. To further increase the power density, reduce the transformer losses, and enhance the heat dissipation capability, multiobjective optimization is developed to meet multiple design requirements simultaneously. A design case is studied to show the advances of the proposed 5P-MIT. To further investigate the proposed 5P-LLC, a down-scaled prototype is developed with a 5P-MIT. Experiments are conducted to verify the analyses and the functionality.**

***Index Terms*—Five-phase LLC (5P-LLC) resonant converter, magnetic integrated transformer, multiobjective optimization.**

I. Introduction

THE LLC resonant converter is a promising topology with the superiority full-load zero-voltage soft-switching (ZVS) capability [1], [2]. It is widely used in medium- and high-power applications such as cascaded H-bridge (CHB) photovoltaic (PV) generation systems [3], [4], modular energy storage systems [5], and electric vehicle charging systems [6], [7]. The high-power LLC resonant converters can not only provide galvanic isolations for distributed power sources but also greatly improve the system efficiency due to the soft-switching capability.

For high-power LLC resonant converters, the transformer plays an important rule, which affects the system overall performance [8], [9]. In single-phase applications, the transformer needs to conduct the rated power, which results in high transformer losses. Certain insulation materials are also required for medium-voltage applications, e.g., in medium-voltage CHB PV systems [3], [4], [10], which further reduces the transformer heat dissipation capability [11]. As a result, a high temperature rise can be generated in the transformer, which deteriorates the system performance [12].

The three-phase LLC converter (3P-LLC) can alleviate the above-mentioned weaknesses [13], [14]. It employs three discrete transformers, which result in a larger core area for a better heat dissipation capability compared with the single-phase counterpart, being a suitable topology for the isolated dc–dc converters in high-power applications [15]. However, discrete magnetic components increase both the volume and weight of a converter system. To further increase the power density of isolated dc–dc converters, magnetic integration is a promising solution [16], [17].

Magnetic integration for LLC resonant converters can be realized in both the component level and the transformer level. The resonant tanks in LLC converters are usually comprised of a series inductance, a parallel inductance, and a transformer. From the component-level perspective, the parallel inductance can be realized with the transformer magnetizing inductance, whose value can be designed by adjusting the air gap [18]. While the series inductance can be realized through the leakage inductance by designing the winding configurations [19]. Thereby, an integration of magnetic components can be realized [20], [21].

From the transformer-level perspective, the discrete transformers and the magnetic components in the resonant tanks can be further integrated, forming a three-phase magnetic integrated transformer (3P-MIT). For integrated transformers, consistent phase parameters are preferred to prevent the current imbalance. In [22], a four-limb 3P-MIT in 3P-LLC is proposed for electric

Manuscript received 20 February 2022; revised 2 May 2022; accepted 26 June 2022. Date of publication 30 June 2022; date of current version 26 July 2022. This work was supported in part by the Chinese National Natural Science Foundation of China under Grant 52077051, in part by the Institute of Energy at Hefei Comprehensive National Science Center under Grant 19KZS207 and Grant 21KZS203, in part by 111 Project under Grant BP0719039, in part by National and Local Joint Engineering Laboratory for Renewable Energy Access to Grid Technology, Hefei University of Technology, Hefei, China. Recommended for publication by Associate Editor Y. Siwakoti. *(Corresponding author: Zhiqing Yang.)*

Jianing Wang, Jiawen Hu, Wei Pei, Zhiqing Yang, and Xing Zhang are with the School of Electrical Engineering and Automation, Hefei University of Technology, Hefei 230009, China (e-mail: jianingwang@hfut.edu.cn; jiawenhu@mail.hfut.edu.cn; weipei@mail.hfut.edu.cn; zhiqing.yang@hfut.edu.cn; honglf@ustc.edu.cn).

Jiacai Zhuang is with Sungrow Power Supply Company, Ltd, Hefei 230088, China (e-mail: zhuangjc@sungrowpower.com).

Color versions of one or more figures in this article are available at https://doi.org/10.1109/TPEL.2022.3187465.

Digital Object Identifier 10.1109/TPEL.2022.3187465

vehicle applications. The center limb is designed with an air gap, which increases the reluctance and the coupling among three outer magnetic limbs. However, an additional limb increases the consumption of the magnetic materials. Noah *et al.* [23] present another four-limb 3P-MIT, the central limb has no air gap, while the outer three limbs have a gas gap to increase the reluctance. Magnetic flux intersects in the central limb to achieve the decoupling. Besides, a balancing transformer is proposed to balance the three-phase resonant current. In [24], a Lagrangian dynamics model is used to analyze the decoupling of the 3P-MIT in [23]. It is proven that the 3P-MIT is feasible to replace three discrete transformers. In [25] and [26], a horizontal three-limb 3P-MIT is developed to save the magnetic materials, following the area product (AP) method. However, the magnetic integration of LLC converters with more than three phases has been seldom investigated.

In high-power LLC resonant converters, e.g., in CHB PV applications, the transformer design needs to meet the requirements of power density, losses, and heat dissipation simultaneously. Therefore, an optimization design for MIT is necessary. Conventionally, the AP method is utilized to design transformers according to the AP values [26]–[28]. However, the power density and transformer losses are usually not fully optimized. An optimal design of a 3.52-kW/20-kHz transformer is presented in [29], considering the losses and the leakage inductance through genetic algorithm. However, the heat dissipation and the power density can be further optimized. The design and optimization of a 166-kW/20-kHz transformer is elaborated in [30], considering the power density and transformer losses, while the heat dissipation performance is neglected. A 1-MW/5-kHz high-power transformer is designed to meets the requirements of efficiency, isolation, and leakage inductance under the limit of temperature rise [31]. However, the power density can be further optimized. For high-power applications, a more comprehensive optimization considering various aspects is preferred, to maximally utilize the integrated transformers.

To further increase the power transfer capability and optimize the performance of the LLC converter, this work investigates the design and optimization of a five-phase magnetic integrated transformer (5P-MIT) in a five-phase LLC (5P-LLC) converter for CHB PV generation systems. The main contributions are summarized as follows:

1) Concrete design process of the 5P-MIT is conducted. A novel limb structure is proposed to prevent local flux distribution. A magnetic circuit model is developed to prove that the 5P-MIT is equivalent to five discrete counterparts. Robustness analysis is conducted to evaluate the impact of reluctance discrepancy.
2) A multiobjective optimization algorithm is proposed for the 5P-MIT, so that the power density, transformer losses, and heat dissipation capability can be designed simultaneously.

The rest of this article is organized as follows. Section II introduces the fundamentals of the 5P-LLC, including the operation principle, the voltage gain, and the parameter design. Section III presents the in-depth design of the 5P-MIT. A staggered limb structure is proposed to prevent local flux saturation. Magnetic circuit models are developed and the robustness against the reluctance discrepancy is investigated. To further optimize the 5P-MIT considering various aspects, a multiobjective algorithm is proposed in Section IV. Design cases are presented to show the advances of the proposed 5P-MIT. To investigate the functionality of the proposed 5P-MIT in the 5P-LLC converter, a down-scaled prototype is developed in Section V. Experiments are conducted to verify the design accuracy. Finally, Section VI concludes this article.

TABLE I
SPECIFICATIONS OF THE 200-KW 5P-LLC CONVERTER

Parameters	U_{in}	P_{N}	N
Value	1300 V	200 kW	1.5

II. 5P-LLC RESONANT CONVERTER

The system configuration of the investigated LLC converter for the medium-voltage CHB PV application is presented in Fig. 1, referring to [3], [4]. The investigated LLC resonant converter is rated at 200 kW with the input voltage of 1300 V and the transformer turns ratio of 1.5, as specified in Table I. A multiphase structure is considered to enhance the power transfer capability. To minimize the current and voltage ripple in the output filter, it is recommended to select an odd phase number. Thus, a 5P-LLC is proposed for the following investigations. To further increase the power density of the converter system, a 5P-MIT is proposed and developed. The fundamentals of the 5P-LLC will be introduced in this section, including the operation principle, the voltage gain, and the parameter design.

A. Operation Principle

As illustrated in Fig. 1, the 5P-LLC consists of five half-bridge converters in parallel, a five-phase resonant tank with the proposed 5P-MIT, five diode half-bridge converters, and dc-side filters. The resonant tank is comprised of five-phase resonant inductance L_{rx} (x = A, B, C, D, E), the magnetizing inductance L_{mx}, and the resonant capacitor C_{rx}. The resonant inductance is realized by the leakage inductance of the 5P-MIT. Since the resonant tank contains two magnetic elements, two resonant frequencies can be obtained as given in (1) and (2). To guarantee the ZVS capability, it is necessary to select the switching frequency f_{s} larger than f_{r2}. Usually, it is preferred to consider f_{s} the same as f_{r1} [2]

$$f_{\text{r1}} = \frac{1}{2\pi\sqrt{L_{\text{rx}}C_{\text{rx}}}} \tag{1}$$

$$f_{\text{r2}} = \frac{1}{2\pi\sqrt{(L_{\text{rx}} + L_{\text{mx}})\,C_{\text{rx}}}}. \tag{2}$$

The 5P-LLC converter is operated with the phase-shift modulation considering a fixed duty cycle of 50% in each bridge. Different from a single-phase or a three-phase LLC resonant converter, the phase-shift angle of the 5P-LLC converter is determined as 72°. Exemplary voltage and current waveforms of

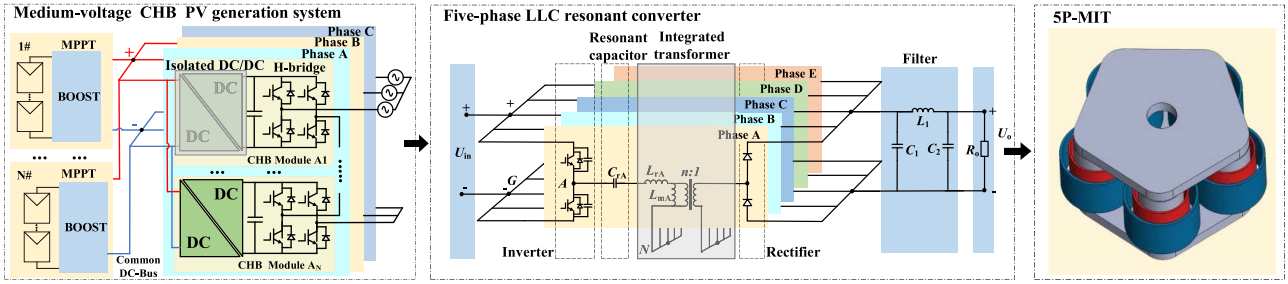

Fig. 1. Configuration of the proposed 5P-LLC resonant converter in the medium-voltage CHB PV application and the proposed 5P-MIT structure.

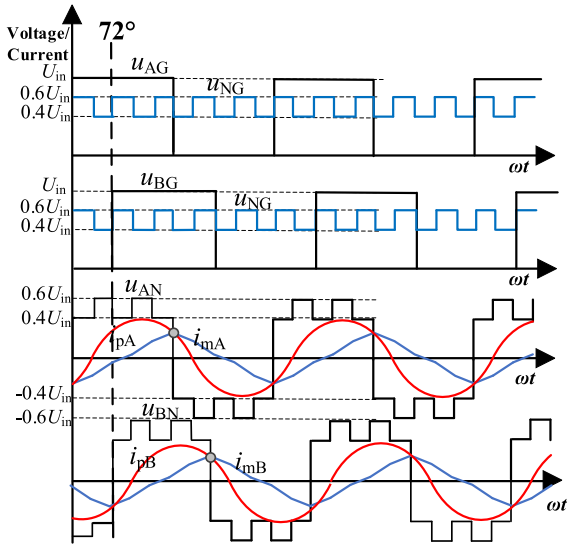

Fig. 2. Steady-state voltage and current waveforms of the 5P-LLC converter.

a 5P-LLC converter are shown in Fig. 2, considering only phase A and B.

Star connection is considered for both the primary and the secondary side of the transformer. Due to the interleaved modulation voltages, the neutral-point voltage $U_{\rm NG}$ alternates as a square form with the frequency of $5f_{\rm s}$, and the amplitude between $0.4U_{\rm in}$ and $0.6U_{\rm in}$, which is determined by the transformer phase voltages.

Due to the resonant tank, the primary-side phase current in the transformer $i_{\rm px}$ presents a sinusoidal form with a frequency of $f_{\rm s}$, which is determined by the magnetizing current $i_{\rm mx}$ and the secondary-side phase current $i_{\rm sx}$ simultaneously. The magnetization current $i_{\rm mx}$ is determined by the primary-side voltage, whose peak value is determined by (3), where $U_{\rm in}$ denotes the input voltage

$$\hat{i}_{\rm mx} = \frac{3 \cdot U_{\rm in}}{25 \cdot L_{\rm mx} \cdot f_{\rm s}} \tag{3}$$

B. Voltage Gain of the 5P-LLC

The voltage gain of the 5P-LLC converter can be derived using the first harmonic approximation (FHA) approach [2], [15]. Assuming that identical parameters are designed for all phases,

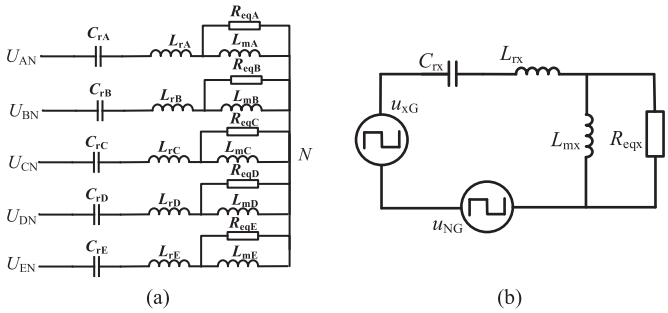

Fig. 3. Equivalent circuit of 5P-LLC. (a) Resonant tank circuit in operation. (b) Equivalent circuit.

an equivalent circuit of the 5P-LLC converter can be obtained, as depicted in Fig. 3. Taking the first harmonic component of the voltage and current in the rectifier bridge, the equivalent load $R_{\rm eqx}$ can be derived as given in (4), where $R_{\rm o}$ is the load resistance, and n denotes the equivalent turns ratio of the 5P-MIT, as given in (5).

$$R_{\rm eqx} = \frac{10}{\pi^2} n^2 R_{\rm o} \tag{4}$$

$$n = N\sqrt{\frac{L_{\rm mx}}{L_{\rm mx} + L_{\rm rx}}}. \tag{5}$$

Hereinafter, and voltage gain M of the 5P-LLC converter can be derived as given in (6), where Q is the quality factor of the 5P-LLC, k is the inductor ratio, and $f_{\rm n}$ is the normalized switching frequency, as specified in (7)

$$M = \frac{nU_{\rm o}}{U_{\rm in}} = \frac{1}{\sqrt{\left(1 + \frac{1}{k} - \frac{1}{kf_{\rm n}^2}\right)^2 + Q^2\left(f_{\rm n} - \frac{1}{f_{\rm n}}\right)^2}} \tag{6}$$

$$k = \frac{L_{\rm mx}}{L_{\rm rx}}, f_{\rm n} = \frac{f_{\rm s}}{f_{\rm r1}}$$

$$Q = \frac{2\pi f_{\rm r1} L_{\rm rx}}{R_{\rm eqx}} = \frac{1}{2\pi f_{\rm r1} C_{\rm rx} R_{\rm eqx}}. \tag{7}$$

Based on (6), the gain curves considering various load conditions are depicted in Fig. 4. In the application of medium-voltage CHB PV systems. The common dc-bus voltage is regulated as constant [3]. To maintain the power balance among each module, it is preferred to keep the output voltage constant as

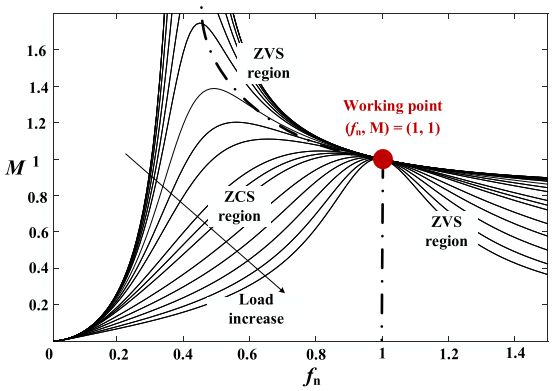

Fig. 4. Gain curve of the 5P-LLC.

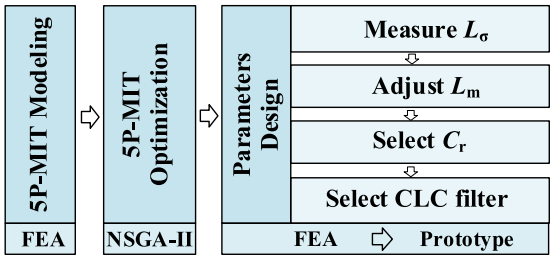

Fig. 5 Design procedure of 5P-LLC converter.

well. According to the operating curves presented in Fig. 4, the gain curve of the 5P-LLC behaves independent of the load condition at the resonant frequency f_{r1}, which is recommended as the nominal operating frequency.

C. Parameter Design

To facilitate the parameter design of the 5P-LLC converter, a design procedure is proposed as illustrated in Fig. 5. A finite element analysis (FEA) model of the 5P-MIT is first developed. Based on that, the flux distributions are investigated to determine the optimal limb structure. Detailed converter dimensions and the resonant frequency are determined through the multiobjective optimization. Hereinafter, the parameters of the resonant tank and the output filter can be further designed and adjusted.

The phase inductances of the 5P-MIT can be extracted based on the developed FEA model. The leakage inductance can be measured by applying an excitation with the secondary-side short-circuit connection, while the magnetization inductance can be estimated with the secondary-side open-circuit connection, respectively.

For the 5P-LLC converter in the CHB PV application, the nominal switching frequency of the 5P-LLC converter is selected as f_{r1}. Thus, the design of the 5P-LLC converter focuses on the inductor ratio k, which affects both the peak magnetizing current and the soft-switching capability.

As depicted in Fig. 2, the peak magnetizing current intersects with the primary-side phase current at the turn-OFF instant. Usually, it is flexible to design L_{mx} rather than L_{rx} by adjusting the air gap. For a given L_{rx}, an increased k reduces the peak magnetizing current, which reduces the turn-OFF losses simultaneously. Besides, an increased k smoothens the gain curve, which benefits the voltage balancing among different half-bridge modules.

To guarantee the soft-switching operation capability, a certain amount of magnetizing current is required to commutate the charge in the output capacitance of semiconductor devices C_{oss} within the dead time T_d, between the upper and lower power devices [2], as given in the following equation:

$$k \leqslant \frac{3 \cdot T_d}{50 \cdot f_s \cdot L_{rx} \cdot C_{oss}} - 1 \tag{8}$$

Considering various impacts on the switching losses, gain curve characteristics, and soft-switching capability, it is preferred to design the value of k between 10 and 15. The length of the air gap can be adjusted to change the value of k in the FEA model. After adjusting the air gap, new values of inductances shall be extracted with the FEA model to facilitate further designs.

Deriving from (1), the capacitance of the resonant tank C_{rx} can be selected according to (9), where the switching frequency f_s is consistent with the resonant frequency f_{r1}

$$C_{rx} = \frac{1}{4\pi^2 L_{rx} f_s^2}. \tag{9}$$

The current distribution of each leg depends on the parameter discrepancy of the five-phase resonant tank. To reduce the current imbalance of the 5P-LLC converter, efforts are made to maintain the parameter consistency for all phases. It is found that an increased value of i_m (a decreased value of L_m) can also result in a higher current imbalance among phases.

To further improve the current distribution capability, a CLC output filter is implemented. The CLC filter consists of a small capacitor C_1, a large capacitor C_2, and an inductance L_1. The large capacitor C_2 is designed for filtering out the ac component. The filter parameters C_1 and L_1 are designed to form a parallel resonance with L_m at the switching frequency, so that the equivalent effect of i_m can be suppressed. The value of C_1 and L_1 shall meet the requirement given in the following equation:

$$f_s = \frac{1}{2\pi\sqrt{\left(\frac{L_{mx} L_{1eq}}{L_{mx} + L_{1eq}}\right) C_{1eq}}} \tag{10}$$

where C_{1eq} and L_{1eq} are the equivalent values of C_1 and L_1 referring to the primary side. Based on the FHA approach, the values of C_{1eq} and L_{1eq} are determined with (11) and (12).

$$C_{1eq} = \frac{\pi^2}{10n^2} C_1 \tag{11}$$

$$L_{1eq} = \frac{10n^2}{\pi^2} L_1. \tag{12}$$

By means of that, the balance of current distributions can be improved, which enhances the operation robustness against the resonant tank parameter discrepancy.

Porotype can be developed after designing the key parameters. The actual values of the leakage inductance and the magnetization inductance shall be measured and compared with the

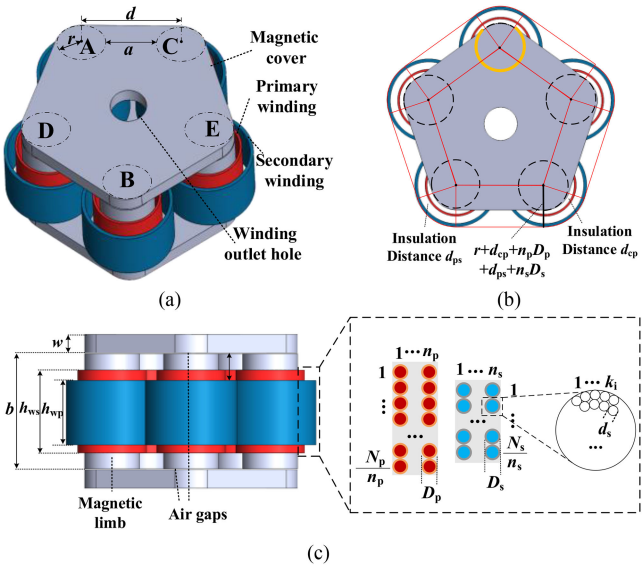

Fig. 6. Detailed parameter labeling of the 5P-MIT. (a) Schematic diagram of 5P-MIT. (b) Top view. (c) Front view of 5P-MIT and schematic diagram of winding.

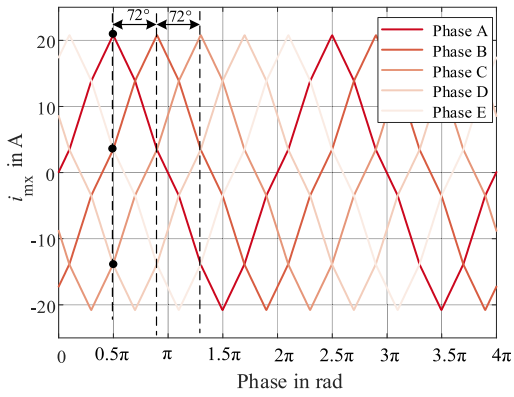

Fig. 7. Magnetizing currents of the 5P-MIT.

estimated values obtained from the FEA model, in order to verify the design accuracy.

III. Design and Modeling of the 5P-MIT

To improve the power density of the 5P-LLC converter, an integrated transformer is designed to fully utilize the magnetic paths. A novel phase structure is proposed to optimize the flux distribution, so that local magnetic saturation can be prevented. Magnetic circuit models are derived to show the equivalent performance of the 5P-MIT comparing to five separated transformers. Robustness analysis is conducted to investigate the impact of the parameter.

A. Structure Design With Flux Optimization

To remain a symmetric geometry, a five-phase integrated transformer is designed in the pentagon form with arc edges. The detailed mechanical structure and winding configurations are described in Fig. 6. The 5P-MIT consists of five identical circular limbs with a radius r. The cores are arranged 72° out of phase with each other with a central distance d. Two magnetic covers are placed at the top and bottom, bridging the common magnetic paths. Nonmagnetic materials of the same thickness are laid between the magnetic covers and individual limbs, to create desired air gaps. The primary- and secondary-side windings are wrapped concentrically on individual limbs, considering a wire diameter $D_{\rm p}$ and $D_{\rm s}$, respectively.

To reduce the core losses in medium- and high-frequency operations, nanocrystalline and ferrite materials are preferred. Nanocrystalline materials have better magnetic performance. However, significant core degradation may occur for nanocrystalline during the cutting process, which restricts the customized applications requiring high manufacture flexibility. Besides, nanocrystalline materials are more expensive than ferrite materials [32]. Therefore, ferrite cores are considered for the limbs and covers to develop the 5P-MIT.

To reduce the winding losses in medium- and high-frequency applications, Litz wire and copper foil are commonly considered. From the cost and manufacture point of view, Litz wires are used as winding materials.

A certain insulation distance is considered between the core and primary-side windings $d_{\rm cp}$, and between the primary- and secondary-windings $d_{\rm ps}$, where the insulation materials are filled for safety reasons. Considering an isolation distance between two adjacent limbs $d_{\rm a}$, the available window width is defined as the following equation, where $n_{\rm p}$ and $n_{\rm s}$ represent the number of winding layers

$$a = 2n_{\rm p}D_{\rm p} + 2n_{\rm s}D_{\rm s} + 2d_{\rm ps} + 2d_{\rm cp} + d_{\rm a}. \tag{13}$$

Comparing to conventional single-phase or three-phase transformers, it is difficult for the 5P-MIT to effectively isolate the outlet wires during the connections due to the pentagonal structure. To facilitate the connection of the inverter and diode stage with different voltage ratings, a winding outlet hole is designed at the center of both covers, so that the primary- and secondary-side windings can be routed separately to corresponding stages.

However, the winding outlet wholes may lead to local flux saturation. The magnetizing currents in the 5P-MIT are presented in Fig. 7. At the moment when the magnetizing current of phase A reaches the positive peak value, the current in phase B and E also remain positive. Whereas, the current in phase C and D are quasi peak value in the negative direction. Due to the intrinsic 72° interval of the five-phase structure, the magnetizing current at the peak instant of any phase has the same direction with two adjacent phases. The overlapping impact can result in flux saturation at the center of the transformer covers.

To investigate the flux distribution, simulations are conducted with the developed FEA model for the moment when $i_{\rm mA}$ reaches the peak value. After extracting the value of $L_{\rm rx}$ and $L_{\rm mx}$, the phase currents $i_{\rm px}$ and $i_{\rm sx}$ can be evaluated based on the FHA approach. The phase currents at the investigated moment are added in the FEA model as excitations. By means of that, the flux distributions can be observed and evaluated. If the limbs are arranged in the clockwise or counterclockwise sequence, the flux density concentrates at the center of the magnetic covers,

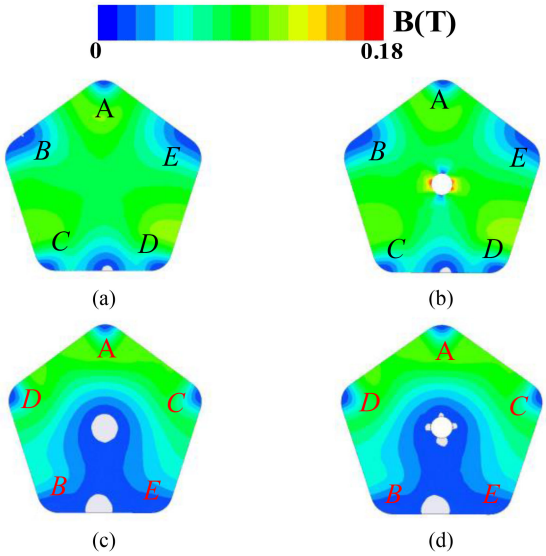

Fig. 8. Flux distribution on the cover considering different limb sequences (consider i_{mA} max). (a) Counterclockwise. (b) Counterclockwise with outlet hole. (c) Staggered. (d) Staggered with outlet hole.

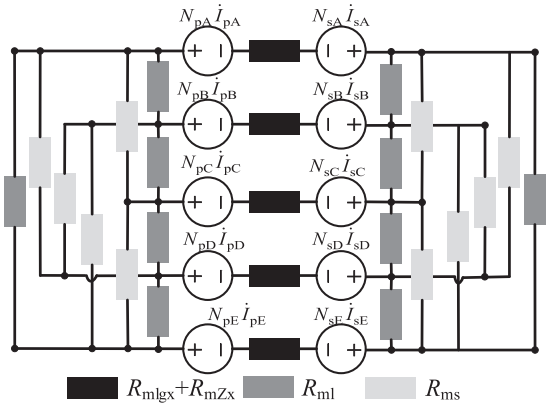

Fig. 9. Equivalent magnetic circuit model of the 5P-MIT.

as shown in Fig. 8(a). Local magnetic saturation can occur if the outlet whole is designed for the windings, as described in Fig. 8(b). To prevent the local flux saturation, a staggered limb sequence is proposed by utilizing the counter effect of nonadjacent phases. By means of that, the flux density at the cover center can be significantly released, as illustrated in Fig. 8(c) and (d). The flux optimization with the staggered limb structure applies to the whole operating period.

B. Magnetic Circuit Modeling

To compare the performance between the magnetic integrated transformer and multiple individual transformers, an equivalent magnetic circuit is required.

Considering the reluctance of each limb R_{mzx}, the reluctance of the air gap R_{mgx}, the reluctance between any two adjacent limbs R_{ms} and opposite limbs R_{ml}, an equivalent magnetic circuit model is developed for the investigated 5P-MIT, as shown in Fig. 9. The reluctance depends on the relative permeability of

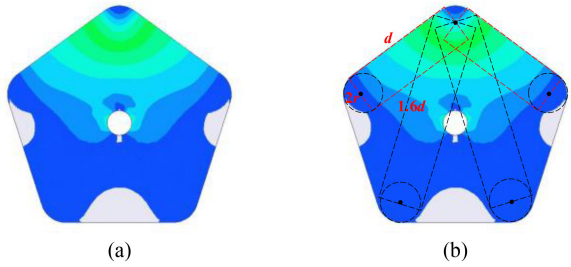

Fig. 10 Flux distribution and path division on the cover with single-phase excitation. (a) Flux distribution. (b) Path division.

the material u_{r} as well as the geometry, i.e., the length and cross-section area [18]. According to the geometry shown in Fig. 6, the reluctances of each limb and the air gap are obtained as given in (14) and (15). Considering the fringing flux in the air gap, the effective cross-section area of the air gap increases, which leads to a decreased reluctance. A coefficient F is considered for the correction, as defined in (16), where l_{gx} denotes the length of the air gap [18]

$$R_{\mathrm{mzx}} = \frac{b}{4\pi^2 \cdot 10^{-7} \cdot u_{\mathrm{r}} \cdot r^2} \tag{14}$$

$$R_{\mathrm{mgx}} = \frac{l_{\mathrm{gx}}}{F \cdot 4\pi^2 \cdot 10^{-7} \cdot r^2} \tag{15}$$

$$F = 1 + \frac{l_{\mathrm{gx}}}{\sqrt{\pi r^2}} \ln\left(\frac{2b}{l_{\mathrm{gx}}}\right). \tag{16}$$

Since the flux intersects with each other in the magnetic covers, the reluctances among adjacent limbs and the opposite limbs are difficult to describe. To define the flux paths in the magnetic covers, FEA simulations are conducted. The flux distribution in magnetic covers can be evaluated by applying a single-phase dc current excitation. Based on that, flux paths are divided to facilitate modeling, as shown in Fig. 10.

According to Fig. 10(a), most of the magnetic flux in the cover flows into the adjacent limbs, while only little flux flows into the opposite side. To facilitate the analysis, the flux distribution is divided into four rectangles, as illustrated in Fig. 10(b). For two of the adjacent limbs, the flux path in the cover is in a rectangle with a width of $2r$ and a length of d. While for the two opposite limbs, the flux path in the cover is in a rectangle with a width of $2r$ and a length of $1.6d$. Meanwhile, to prevent the magnetic density in the covers from exceeding B_{m}. The cross-section when the magnetic flux flows from the limb into the covers is defined, which is a cylindrical surface with a height w and an arc length of $1.4\pi r$, as highlighted with the orange arc in Fig. 6(b). The highlighted area is assumed to be equal to the cross-section of the limb. Based on that, the height of the covers w can be evaluated as $5r/7$. Hence, the reluctance between the adjacent limbs and the opposite limbs in the covers R_{ms} and R_{ml}, can be obtained as follows:

$$R_{\mathrm{ms}} = \frac{d}{8\pi \cdot 10^{-7} \cdot u_{\mathrm{r}} \cdot w} \tag{17}$$

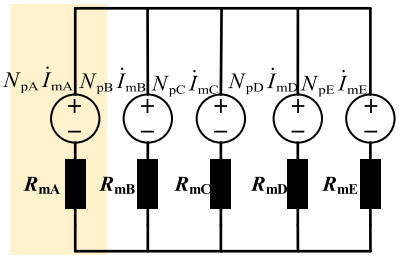

Fig. 11. Equivalent magnetic circuit.

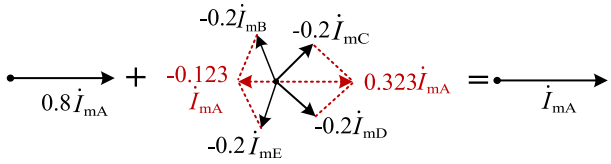

Fig. 12. Phasor diagram of the magnetizing currents of (20).

$$R_{ml} = \frac{d}{5\pi \cdot 10^{-7} \cdot u_r \cdot w}. \tag{18}$$

Since individual reluctances are obtained, the equivalent phase reluctance R_{mx} can be derived according to Fig. 9 by combing (14)–(18), as given in (19). Hereinafter, the simplified equivalent magnetic circuit seen from the primary side is obtained, as depicted in Fig. 11

$$R_{mx} = R_{mgx} + R_{mzx} + \frac{(2R_{ml} + R_{mzx})(2R_{ms} + R_{mzx})}{4R_{ml} + 4R_{ms} + 4R_{mzx}}. \tag{19}$$

Each phase of the 5P-MIT can achieve an equivalent performance comparing to a single-phase counterpart. According to Fig. 11, the flux linkage of the secondary-side windings in a single phase (take phase A as an example) can be calculated with (20). Assuming that the 5P-MIT is designed in balance, identical reluctance R_m and current magnitude are obtained for all phases. According to the phasor diagram of magnetizing currents depicted in Fig. 12, (20) can be further simplified to (21), which indicates that the flux performance of a single limb is equal to a single-phase transformer (SPT). It is proved that the 5P-MIT can achieve the consistent performance of five single-phase discrete transformers once the phase parameters are designed as balanced

$$\psi_{sA} = \frac{N_p N_{sA}}{R_m}\left[\frac{4\dot{I}_{mA}}{5} - \frac{1}{5}\sum_{i=B,C,D,E}^{i} \dot{I}_{mi}\right]$$

$$= \frac{N_p \dot{I}_{mA} N_s}{R_m} \tag{20}$$

$$= \frac{N_p \dot{I}_m N_s}{R_m}. \tag{21}$$

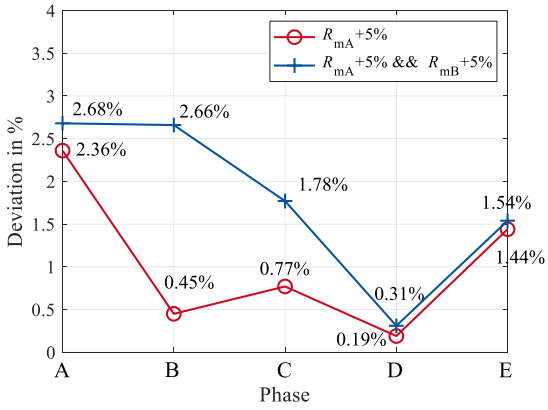

Fig. 13. Phase current deviation considering different R_{mx} discrepancy.

C. Robustness Analysis

For multiphase applications, the imbalance of reluctances among phases may challenge the performance. Thus, robustness analysis is conducted to investigate the impact of parameter discrepancy. In practice, the reluctance of each phase R_{mx} has a certain deviation to the nominal value, which affects the phase currents of 5P-LLC.

To analyze the system robustness, two different cases are studied to evaluate the phase current deviations through FEA simulations. The first case considers that one of the reluctances has a 5% deviation. Due to symmetric structure of the 5P-MIT, the reluctance of phase A R_{mA} is considered as an example. As depicted in Fig. 13, the deviation of R_{mA} results in current deviations in all phases. It is reasonable that the maximum current deviation to the nominal value occurs in phase A. The second case considers that two of the reluctances have both 5% deviations, e.g., in phase A and B, which leads to most current deviations in the corresponding phases. However, the maximum phase current deviations are less than 3% of the ideal value, which verifies the robustness of the designed 5P-MIT against the parameter deviations.

IV. Multiobjective Optimization

Although the power density is enhanced through the magnetic integration, other aspects may still challenge the transformer performance, i.e., the transformer losses and the heat dissipation capability. To comprehensively improve the transformer performance, a multiobjective optimization method is proposed by utilizing the evolutionary algorithm. The design case is presented for a 200-kW 5P-MIT.

A. Optimization Objectives

One of the challenges in the transformer design is to achieve high power density while reserve enough heat dissipation capability simultaneously. To cope with this challenge, a multiobjective optimization method is proposed, which considers the power density, transformer losses, and heat dissipation capability simultaneously.

1) Power Density: Power density represents the integration level of a magnet-integrated transformer, which is estimated through the nominal power P_{N} and the transformer volume V_{tr} (22). According to the designed geometry shown in Fig. 4, the volume of the 5P-MIT can be evaluated with (23)

$$\gamma = \frac{P_{\mathrm{N}}}{V_{\mathrm{tr}}} \tag{22}$$

$$V_{\mathrm{tr}} = \Big[1.72d^2 + \pi(r + n_{\mathrm{p}}D_{\mathrm{p}} + n_{\mathrm{s}}D_{\mathrm{s}} + d_{\mathrm{ps}} + d_{\mathrm{cp}})^2 + 5d \cdot (r + n_{\mathrm{p}}D_{\mathrm{p}} + n_{\mathrm{s}}D_{\mathrm{s}} + d_{\mathrm{ps}} + d_{\mathrm{cp}})\Big] \cdot (b + 2w)\,. \tag{23}$$

2) Transformer Losses: The transformer losses are comprised of the core losses P_{core} and the winding losses P_{winding}. Since the phase voltages of the 5P-MIT are nonsinusoidal signals, the waveform coefficient Steinmetz equation is adopted to estimate the core losses, as given in (24) [33]. K, α, and β are constant coefficients depending on the core material. V_{core} represents the core volume, and B_{m} is the maximum magnetic flux density in one limb, which is determined by the phase voltage U_{pri}, the switching frequency f_{s}, the number of turns of primary-side windings N_{p}, and the cross-section area of the magnetic limb A_{e}, as given in (25). Higher phase voltages or a higher switching frequency can lead to increased transformer core losses

$$P_{\mathrm{core}} = \frac{9\pi \cdot K \cdot f_{\mathrm{s}}^{\alpha} \cdot B_{\mathrm{m}}^{\beta} \cdot V_{\mathrm{core}}}{35} \tag{24}$$

$$B_{\mathrm{m}} = \frac{U_{\mathrm{pri}}}{4.082 \cdot f_{\mathrm{s}} \cdot N_{\mathrm{p}} \cdot A_{\mathrm{e}}}. \tag{25}$$

To calculate the winding losses of Litz wires, the dc resistances R_{dci} ($i = p,s$) are first evaluated according to (26) and (27) for both primary and secondary sides, where K_{w} is the ratio of the actual conduction copper area to the overall cross-sectional area of the Litz wire, k_{i} is the number of strands of the Litz wire, d_{s} is the diameter of a single strand of the Litz wire, MLT_{i} is the average turn length of windings, and ρ is the resistivity of the Litz wire

$$R_{\mathrm{dci}} = \frac{4 \cdot \rho \cdot N_{\mathrm{i}} \cdot MLT_{\mathrm{i}}}{\pi \cdot k_{\mathrm{i}} \cdot K_{\mathrm{w}} \cdot D_{\mathrm{i}}^2} \tag{26}$$

$$D_{\mathrm{i}} = \sqrt{\frac{d_{\mathrm{s}}^2 k_{\mathrm{i}}}{K_{\mathrm{w}}}}. \tag{27}$$

Hereinafter, the ac resistances can be estimated by multiplying the dc resistances and the ac resistance factor F_{Ri}, according to the Dowell model. For the developed 5P-MIT, the windings are placed far away from the air gap to reduce the losses caused by the air gap effect. Due to the high insulation requirements, insulation distance shall be left between the covers and the windings. Hence, the porosity of windings is small, resulting in deviations of the Dowell model. To improve the accuracy, the Rogowski correction factor is introduced to correct the ac resistance factor by modifying the window height, as given in (28)–(30). A_{i} denotes the normalized ratio of the single-strand diameter to the skin depth of the Litz wire, n_{i} is the number of winding layers, δ is the skin depth of a single strand of the Litz wire, ξ_{i} is the porosity of the winding, and b_{eqi} is the corrected window height [19]

$$F_{\mathrm{Ri}} = A_{\mathrm{i}} \left[\frac{\sinh(2A_{\mathrm{i}}) + \sin(2A_{\mathrm{i}})}{\cosh(2A_{\mathrm{i}}) - \cos(2A_{\mathrm{i}})} + \frac{2\left(k_{\mathrm{i}} n_{\mathrm{i}}^2 - 1\right)}{3} \cdot \frac{\sinh(A_{\mathrm{i}}) - \sin(A_{\mathrm{i}})}{\cos(A_{\mathrm{i}}) + \cos(A_{\mathrm{i}})} \right] \tag{28}$$

$$A_{\mathrm{i}} = \left(\frac{\pi}{4}\right)^{0.75} \cdot \frac{d_{\mathrm{s}}}{\delta} \cdot \sqrt{\xi_{\mathrm{i}}} \tag{29}$$

$$\xi_{\mathrm{i}} = \frac{N_{\mathrm{i}} \cdot \sqrt{k_{\mathrm{i}}} \cdot d_{\mathrm{s}}}{b_{\mathrm{eqi}}}. \tag{30}$$

Taking both the primary- and secondary-side winding losses for all phases into account, the winding losses can be estimated according to (31). Higher phase currents can lead to increased winding losses

$$P_{\mathrm{winding}} = 5 \cdot F_{\mathrm{RP}} \cdot R_{\mathrm{dcp}} \cdot I_{\mathrm{p}}^2 + 5 \cdot F_{\mathrm{RS}} \cdot R_{\mathrm{dcs}} \cdot I_{\mathrm{s}}^2. \tag{31}$$

3) Heat Dissipation: An increased power density also challenges the heat dissipation capability of transformers, especially with the magnetic integration technique. It is difficult to accurately estimate the temperature rise in a transformer. However, the temperature rise can be roughly evaluated according to (32), depending on the transformer total losses P_{tot} and the surface area S [34]

$$\Delta T = \left(\frac{P_{\mathrm{tot}}}{S}\right)^{0.833}. \tag{32}$$

To quantify the heat dissipation capacity and to facilitate the optimization procedure, the heat dissipation capability is defined as (33), considering the dissipation area and the total losses of a transformer. For the developed 5P-MIT, S can be evaluated by (34) according to the developed geometry

$$S_{\mathrm{heat}} = \frac{S}{P_{\mathrm{tot}}} = \frac{S}{P_{\mathrm{core}} + P_{\mathrm{winding}}} \tag{33}$$

$$S = 5 \cdot \left(\frac{N_{\mathrm{p}}}{n_{\mathrm{p}}} D_{\mathrm{p}} MLT_{\mathrm{p}} + \frac{N_{\mathrm{s}}}{n_{\mathrm{s}}} D_{\mathrm{s}} MLT_{\mathrm{s}}\right) + 10\pi r b + 6.9 \cdot (a + 2r)^2 + \frac{190r}{7} \cdot (a + 2r)^2 - \frac{32}{7}\pi r^2. \tag{34}$$

B. Optimization Algorithm

After determining the optimization objectives, an optimization method is proposed based on the genetic algorithm NSGA-II [35]. As illustrated in Fig. 14, the optimization consists of three main processes, which are the preprocessing, optimization, and design selection.

First, the operating environment of the transformer is clarified, including the rated power, the operating frequency, the voltage and current ratings, and the turns ratio. According to the selected core and winding, material and geometry-related parameters are also defined. The limb cross-sectional radius, the transformer height, the number of turns, the number of layers, and the number

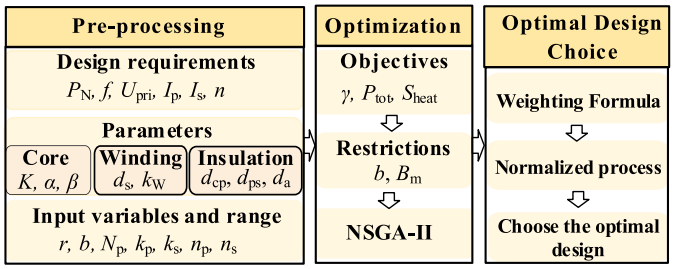

Fig. 14. Optimization design algorithm.

of strands in Litz wires are considered as input variables, whose ranges are predefined according to the available choices in the market.

The defined input variables and the fundamental information of the transformer are sent to a developed mathematical model for optimization. Geometric and magnetic constraints are considered as given in (35). The over optimization goal is selected as (36), so that both the power density and the heat dissipation capability can be maximized, while the transformer losses can be minimized

$$\begin{cases} b - h_{ws} \geqslant 2d_{ps} \\ B_m \leqslant 0.5B_{sat} \end{cases} \tag{35}$$

$$\begin{cases} f_1 = \max(\gamma) \\ f_2 = \min(P_{tot}) \\ f_3 = \max(S_{heat}) \end{cases}. \tag{36}$$

The pareto solution sets are obtained after optimization. To facilitate the design selection considering multiple objectives with different units, the objectives in the pareto solutions are normalized to the corresponding average value with a weighting factor. For integrated transformers, an increased power density may lead to the reduced surface area, affecting the heat dissipation capability. In this work, both the power density and transformer losses are weighted as 0.3, while the heat dissipation capability is slightly more weighted as 0.4, which leads to an evaluation factor m_n as defined in (37). Based on that, final solutions can be determined

$$m_n = 0.3 \cdot \frac{f_{1n}}{f_{1-ave}} - 0.3 \cdot \frac{f_{2n}}{f_{2-ave}} + 0.4 \cdot \frac{f_{3n}}{f_{3-ave}}. \tag{37}$$

C. Optimization Case

Based on the developed optimization method, the multiobjective optimization is implemented for a 200-kW 5P-MIT. System specifications are provided in Appendix. To reduce the core losses and remain a low loss variation for a wide temperature range, TDK's PC95 type ferrite is considered as the core material. The Litz wire with a strand diameter of $d_s = 0.15$ mm is considered for windings, which is suitable for high-frequency operations up to 200 kHz.

To achieve high power density while remaining reasonable losses simultaneously, four different resonant frequencies are investigated, i.e., 15, 30, 45, and 60 kHz. The converter is operated at the resonant frequency. To determine the optimal resonant frequency, optimization objectives are normalized to

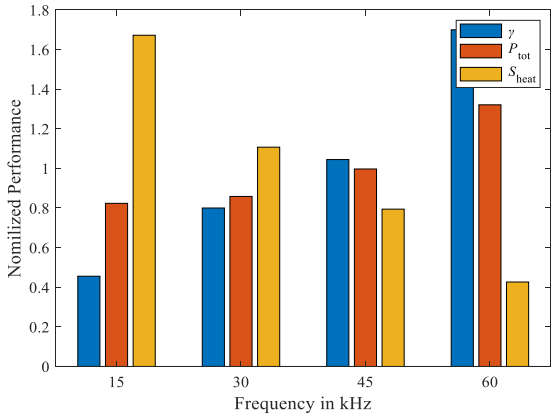

Fig. 15. Optimized designs of 5P-MIT with different resonant frequencies.

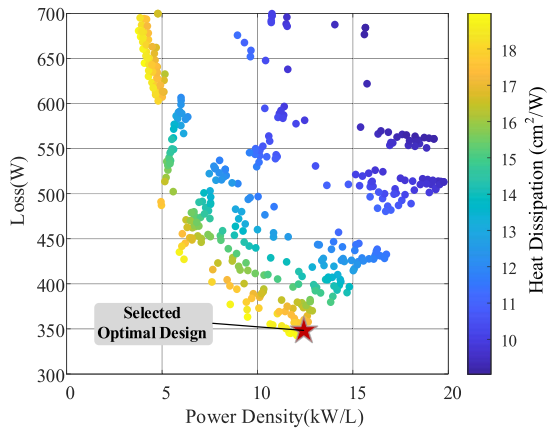

Fig. 16. Pareto-optimal solutions of 5P-MIT ($f_s = f_{r1} = 30$ kHz).

TABLE II
RESONANT TANK PARAMETERS OF THE 200-KW SYSTEM

Phase	A	B	C	D	E	Mean
L_σ (μH)	10.88	10.89	10.89	10.86	10.89	10.88
L_m (μH)	165.29	165.39	165.26	165.21	165.53	165.34
C_r (μF)	/	/	/	/	/	2.59

corresponding average values, and compared with each other, as shown in Fig. 15. With an increased resonant frequency, both the power density and transformer losses increase, while the heat dissipation capability decreases. To maintain a balance among various aspects and ensure a sufficient heat dissipation capability, the resonant frequency is determined as 30 kHz. The pareto solutions output by the NSGA-II are illustrated in Fig. 16. According to the evaluation factor m_n, the optimal design of the 5P-MIT is selected. Detailed design results are provided in Appendix.

The resonant frequency and the dimensions of the 5P-MIT are determined after the optimization. Hereinafter, the magnetizing and leakage inductances can be extracted based on the FEA model, which are given in Table II. According to the mean value of L_{rx}, the resonant capacitor C_r is selected according to (9). The parameters of the CLC filter are determined based

TABLE III
KEY DIMENSIONS AND PERFORMANCE OF DIFFERENT DESIGNS

	Optimized 5P-MIT	Optimized SPT	Optimized 5P-SPT	Non-optimized 5P-MIT
V_{core} (dm^3)	5.81	2.59	8.16	9.21
V_{tr} (dm^3)	16.04	15.55	26.70	21.63
L_{litz} (m)	25.70	104.03	28.94	19.69
S (cm^2)	6114.71	4242.30	8173.94	6935.49
P_{tot} (W)	353.86	508.06	485.10	381.49
γ (kW/dm^3)	12.47	12.86	7.48	9.25
S_{heat} (cm^2/W)	17.28	8.35	16.85	18.18

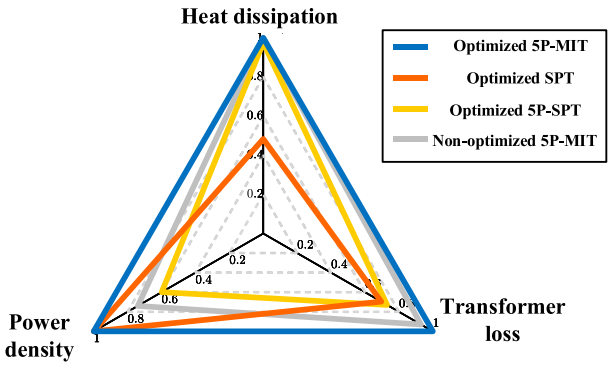

Fig. 17. Comparison among the optimized 5P-MIT, the optimized SPT and the optimized 5P-SPT and the nonoptimized 5P-MIT.

on the mean value of L_{mx} following (10)–(12), which are selected as 3 μF, 10.5 μH, and 500 μF. After determining the key parameters, FEA cosimulations are conducted to further investigate the performance of the 5P-MIT and the 5P-LLC converter.

To show the advancement of the magnetic integration design, an SPT for a full-bridge LLC converter with the same rating and five discrete single-phase transformers (5P-SPT) for the 5P-LLC are designed following the proposed optimization procedure. To investigate the improvement with the optimization process, the 5P-MIT is also designed with the conventional AP method following [28]. Detailed design results of the 5P-MIT, SPT, and 5P-SPT are given in Appendix.

The key dimensions and performance of all designs are compared in Table III. The optimized 5P-MIT requires the second least core volume V_{core} and the Litz wire length L_{litz}, which indicates a low transformer weight and low production cost. As for the transformer performance, optimization objectives are normalized referring to the optimized 5P-MIT, as illustrated in Fig. 17. Note that the transformer losses are compared with the reciprocal values. Among all design cases, the optimized 5P-MIT presents the best overall performance with regard to the heat dissipation, the power density, and transformer losses, which shows the advantages of the magnetic integration. Comparing to the conventional AP method, the power density of the 5P-MIT can be further improved through the multiobjective optimization, and the transformer losses can be reduced as well, which proves the validity of the proposed optimization approach.

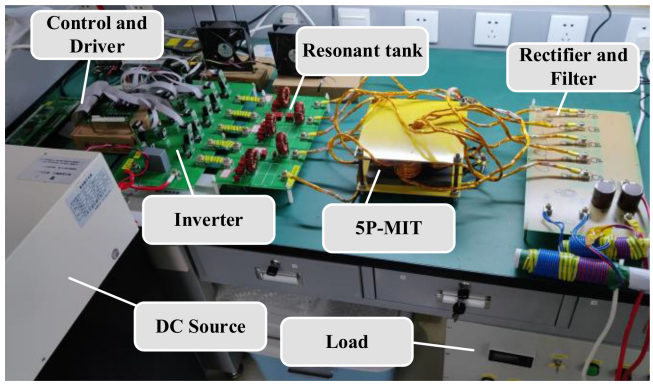

Fig. 18. Experimental setup.

TABLE IV
SPECIFICATIONS OF THE DOWN-SCALED SYSTEM

Parameters	Value	Parameters	Value
U_{in} (V)	260	I_p (A)	6.8
P_N (kW)	3.2	I_s (A)	8.5
f (kHz)	32	d_{cp} (mm)	1
N	1.5	d_{ps} (mm)	2
U_{pri} (V)	129	d_a (mm)	5
Core type	PC95	d_s (mm)	0.15

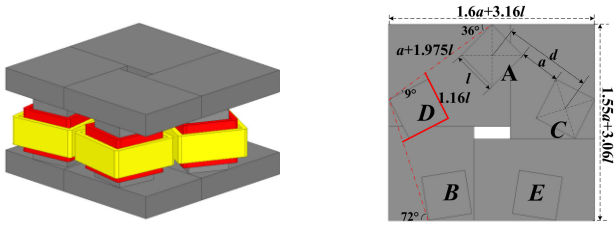

Fig. 19. Schematic of the down-scaled 5P-MIT prototype. (a) Overview. (b) Dimensions in the top view.

V. EXPERIMENTAL VERIFICATION

To further investigate the proposed design of the 5P-MIT and the functionality of the 5P-LLC resonant converter, experiments are conducted based on a developed down-scaled prototype. As illustrated in Fig. 18, the test setup consists of a dc-source, a five-phase inverter stage, a five-phase resonant tank, a 5P-MIT, a five-phase diode rectifier, and the control and driver circuits. The system specifications of the 5P-LLC converter are given in Table IV.

The 5P-MIT is designed and optimized following the same methodology in Sections III and IV. Detailed design results are provided in Appendix. To facilitate the laboratory construction, the cross-sections of the limbs and covers are changed to a square form instead of round shape, which are limited by the available commercial products on the market, as presented in Fig. 19. In the meanwhile, the section radius r, as the input variable during the optimization, is replaced with the section side length l. Note that the models to calculate optimization objectives are updated

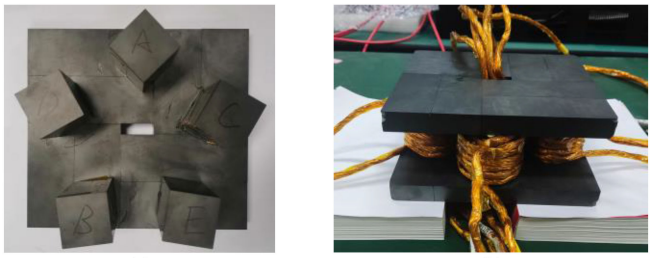

Fig. 20. Constructed down-scaled 5P-MIT prototype. (a) Core overview. (b) Prototype.

TABLE V
RESONANT TANK PARAMETERS OF THE DOWN-SCALED SYSTEM

Phase	A	B	C	D	E	Mean
L_σ (μH)-FEA	2.61	2.62	2.62	2.62	2.62	/
L_σ(μH)-actual	2.46	2.7	2.64	2.33	2.44	/
L_r (μH) Ext.	8.21	8.58	7.91	7.72	8.08	/
L_σ+L_r (μH)	10.67	11.28	10.55	10.05	10.52	10.61
L_m (μH)-FEA	159.34	159.92	160.75	165.14	163.13	161.66
L_m(μH)-actual	164.59	158.19	148.49	171.96	146.59	157.96
C_r (μF)	/	/	/	/	/	2.27

accordingly. The dimensions of the 5P-MIT are obtained after the optimization. Based on that, a prototype is constructed, as depicted in Fig. 20.

A. Measurement of $L_{\sigma x}$ and L_{mx}

The parameter discrepancy among individual phases has an impact on the current balance for the 5P-MIT. To investigate the construction accuracy and the parameter deviation, the leakage inductance and magnetizing inductance of all phases are measured with the E5061B network analyzer. The measured values and the FEA simulated values are compared in Table V. The inductances are slightly different among five phases in FEA simulations, which are caused by the net division of finite elements during the simulations. As windings are wound by hand, deviations are inevitable between the measured values of the prototype and the FEA simulation results. However, deviations are in an acceptable range.

The preliminary designed leakage inductance is only around 2 μH for each phase. If the inductor ratio is designed in the range of 10–15 as recommended in Section II, a large air gap is required, which leads to high magnetizing currents due to a small magnetization inductance. To increase the magnetizing inductance while maintaining the inductor ratio, an external inductance is connected to increase the equivalent resonant inductance. By means of that, the magnetizing inductance can be designed with much higher values and the air gap can be reduced simultaneously.

A CLC filter is also designed and implemented for the down-scaled prototype to balance the current distribution among phases. Following the design rules proposed in Section II, the parameters of the CLC filter are determined as 2 μF, 12.7 μH, and 940 μF, respectively.

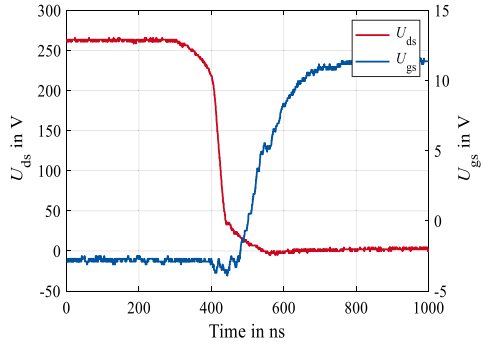

Fig. 21. Drain-source and gate-source voltages in a switching transient.

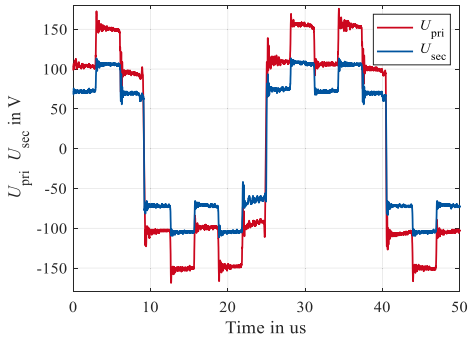

Fig. 22. Phase voltages across the 5P-MIT (phase A).

B. No-Load Test

To investigate the soft-switching capability, the switching transient is investigated for the no-load condition. Since all semiconductors in the 5P-LLC converter are operated with a fixed 50% duty cycle, the switching transient is observed considering only the upper device in a half bridge. As depicted in Fig. 21, the drain-source voltage $U_{\rm ds}$ drops to zero before the gate-source voltage $U_{\rm gs}$ rising to the threshold value, which indicates the ZVS capability during the transients.

Additionally, the voltage across the primary and secondary winding are shown in Fig. 22. The waveforms consist of the working principle shown in Fig. 2, which validates the functionality of the 5P-LLC resonant converter.

C. On-Load Test

To investigate the power transfer capability, on-load tests are conducted for different load conditions. The phase currents of the 5P-LLC resonant converter for 10%, 50%, and 100% load conditions are depicted in Fig. 23(a)–(c). Deviations among phase currents are observed, which are mainly induced by the parameter discrepancy of the 5P-MIT among different phases. The output dc voltages for different load conditions are shown in Fig. 23(d)–(f). At the resonant frequency, the ideal output voltage without considering the voltage drop on the semiconductors shall be 175.6 V according to (6). The output voltage shall remain constant for various load conditions. The measured dc voltages are close to the desired value, which validates the accuracy of the derived voltage gain. With an increased load, the output dc

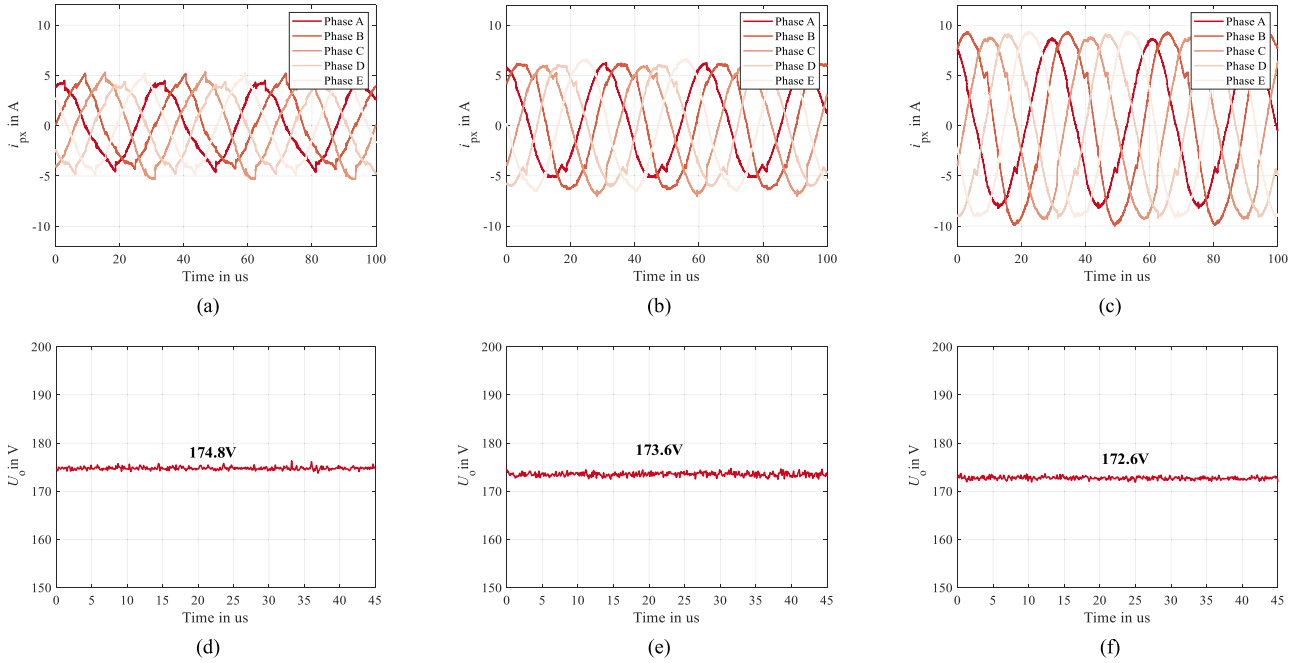

Fig. 23. Resonant currents and output dc voltage with different loads. (a) Resonant currents with 10% load. (b) Resonant currents with 50% load. (c) Resonant currents with 100% load. (d) Output dc voltage with 10% load. (e) Output dc voltage with 50% load. (f) Output dc voltage with 100% load.

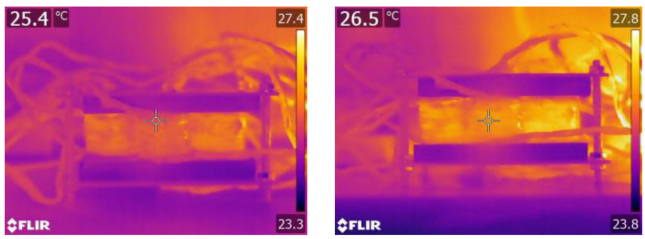

Fig. 24. Thermal images at different operating time. (a) After 5-min operation. (b) After 30-min operation.

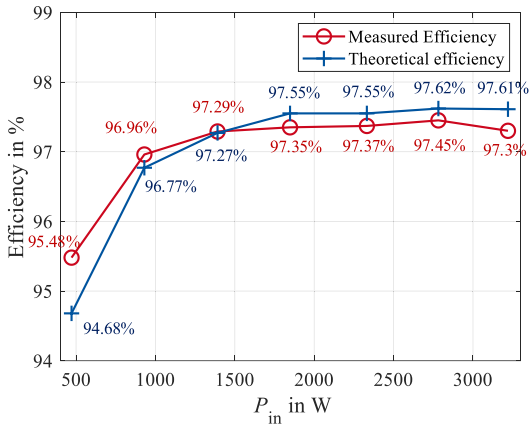

Fig. 25. Comparison between the measured and theoretical efficiency.

voltage slightly decreases due to a higher voltage drop on the semiconductors and passive elements.

To investigate the heat dissipation capability of the developed 5P-MIT, thermal images are recorded for the full load condition. The thermal images after running for 5 and 30 minutes are shown in Fig. 24. After around 30-min full-load operation, only a small temperature rise is observed, which proves the heat dissipation capability of the 5P-MIT.

Since the power losses of the 5P-LLC converter depends on the transformer losses and affects the heat dissipation capability during the optimization. The accuracy of the power loss model is validated by comparing the efficiency curves of the measured and the model-based theoretical values.

The developed loss model considers the on-state losses $P_{\text{on-mos}}$ and the turn-off losses $P_{\text{off-mos}}$ of the power MOSFETs, the on-state losses of the diode in the rectifier $P_{\text{on-dio}}$, the losses of resonant capacitors P_{cr}, the core losses P_{coreL} and the winding losses P_{windingL} of the external inductance, the core losses P_{core} and the winding losses P_{winding} of the 5P-MIT. The on-resistance value of the MOSFETs $R_{\text{ds(on)}}$ and the forward voltage of the diodes V_{F} are calculated with typical values. In practice, $R_{\text{ds(on)}}$ and V_{F} have positive temperature characteristics, resulting in slight deviations between the measured and theoretical values. The measured efficiency and the theoretical efficiency obtained from the loss model consist of each other for a wide operating range, as depicted in Fig. 25, which proves the accuracy of the developed loss model.

Based on the efficiency curve, detailed loss distributions are investigated considering the light-load, half-load, and full-load operations, as illustrated in Fig. 26. For the light-load condition, the transformer core losses dominate the total losses of the 5P-LLC resonant converter. With an increased operating power, the core losses remain almost unchanged, while the on-state losses of both MOSFETs and diodes increase significantly. The external

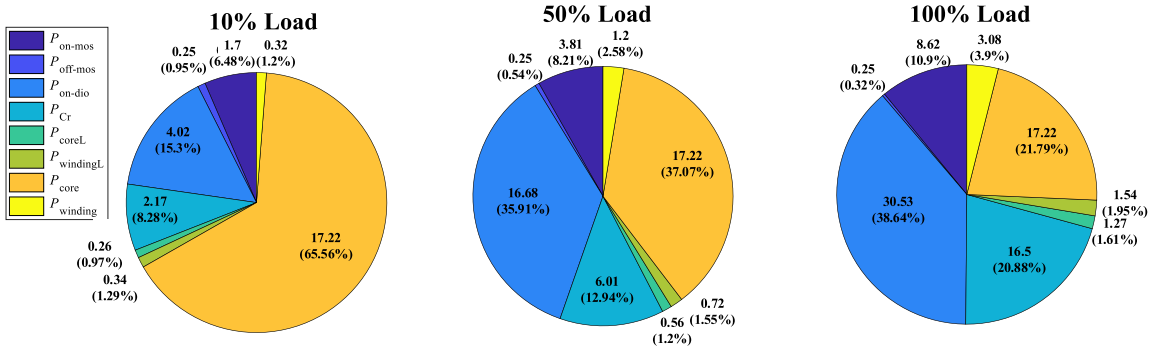

Fig. 26. Loss distribution under different loads.

series inductor only contributes a small amount of loss ratio in the converter level for the whole operation range. With an increased power, the losses induced by the resonant capacitors shall be considered.

VI. Conclusion

This article proposes a 5P-MIT in the 5P-LLC for CHB PV applications. The voltage gain of the 5P-LLC is derived based on the FHA approach. Design procedures of the converter are elaborated, including the analyzes based on the FEA model, the design of the resonant tank, and the output filter. A novel limb structure is proposed to prevent local flux saturation. The magnetic circuit model is developed to prove that the 5P-MIT is equivalent to five discrete counterparts. Robustness analysis is conducted to evaluate the impact of the reluctance discrepancy. Besides, a multiobjective optimization algorithm is proposed for the 5P-MIT, so that the power density, transformer losses, and heat dissipation capability can be optimized simultaneously. Design cases are presented to show the advances of the proposed 5P-MIT and the validity of the proposed multiobjective optimization method. A down-scaled prototype is developed to investigate the functionality of the proposed 5P-MIT and the 5P-LLC resonant converter. Experiments are conducted to analyze the performance and loss distribution of the 5P-LLC converter.

Appendix

Detailed transformer design results for the 200-kW converter system are presented in Appendix A-C, considering the optimized 5P-MIT, the nonoptimized 5P-MIT designed with the AP method, the optimized SPT, and the optimized 5P-SPT. The transformer design results for the down-scaled prototype are presented in Appendix D.

A. Design of the 5P-MIT

System specifications of the 200 kW system are provided in Table VI, including electrical parameters, the core and winding materials. The optimized design results are given in Table VII.

To validate the proposed optimization approach, the 5P-MIT is also designed following the AP method, as introduced in [28]. The product of the core window area A_w and the limb cross-sectional area A_e shall be selected larger than the AP value calculated in (38). $\sum VA$ is the sum of the input and output power of the 5P-MIT, K_v is the waveform factor, K_t is a constant coefficient, and k_u is the window utilization rate. The design results with the AP method are given in Table VIII

$$AP = \left(\frac{\sqrt{2} \sum VA}{K_v f B_m K_t \sqrt{k_u \Delta T_{max}}} \right)^{\frac{8}{7}} \tag{38}$$

TABLE VI
Specifications of the 200-kW Converter System

Electrical	Value	Core	Value	Windings	Value
I_p (A)	66	Type	PC95	d_s (mm)	0.15
I_s (A)	96	K	0.94	K_W	0.55
U_{pri} (V)	662	α	1.453	d_{cp} (mm)	5
		β	2.325	d_{ps} (mm)	15
				d_a (mm)	10

TABLE VII
Optimized Design of the 5P-MIT

Parameters	5P-MIT	Parameters	5P-MIT
r (mm)	37	V_{tr} (dm^3)	16.04
b (mm)	89	S (cm^2)	6114.71
N_p	9	P_{core} (W)	145.48
k_p	1200	$P_{winding}$ (W)	208.38
k_s	1644	P_{tot} (W)	353.86
n_p	1	γ (kW/dm^3)	12.47
n_s	1	S_{heat} (cm^2/W)	17.28

TABLE VIII
Nonoptimized Design of the 5P-MIT With AP Method

Parameters	Value	Parameters	Value
r (mm)	45	V_{tr} (dm^3)	21.63
b (mm)	80	S (cm^2)	6935.49
N_p	6	P_{core} (W)	237.75
k_p	1230	$P_{winding}$ (W)	143.71
k_s	1760	P_{tot} (W)	381.46
n_p	1	γ (kW/dm^3)	9.25
n_s	1	S_{heat} (cm^2/W)	18.18

B. Design of the SPT

To show the advances in the magnetic integration, an SPT of the same rating for a full-bridge LLC resonant converter is

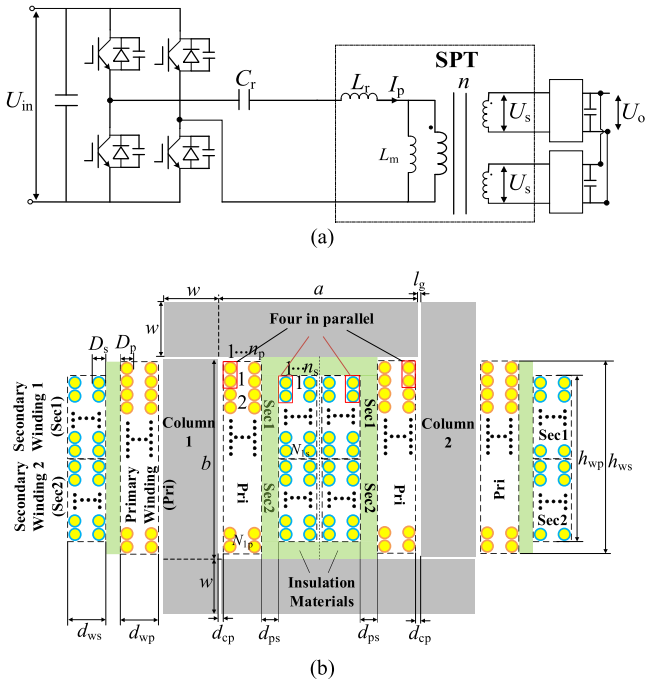

Fig. 27. Schematic diagram of the full-bridge LLC resonant converter and SPT. (a) Full-bridge LLC resonant converter. (b). SPT.

TABLE IX
OPTIMIZED DESIGN OF THE SPT

Parameters	Value	Parameters	Value
a (mm)	135	V_{tr} (dm^3)	15.55
b (mm)	190	S (cm^2)	4242.30
w (mm)	40	P_{core} (W)	103.3
h	2	$P_{winding}$ (W)	404.76
N_p	21	P_{tot} (W)	508.06
k_p	1200	γ (kW/dm^3)	12.86
k_s	630	S_{heat} (cm^2/W)	8.35
n_p	2		
n_s	2		

also designed with multiobjective optimization. The full-bridge LLC converter is illustrated in Fig. 27(a), where the winding of the SPT is comprised of a primary winding and two identical secondary windings, as depicted in Fig. 27(b). Note that the primary-side voltages of the SPT are square waves. As for the transformer construction, the magnetic core is spliced by multiple magnetic blocks with a cross-sectional side length of w. The blocks are spliced along the thickness direction of the magnetic core, the number is h. The air gap l_g is set at the joint of the magnetic blocks. The winding adopts a dual-limb winding structure. The primary and secondary windings are divided into the same two parts and wound on column 1 and column 2 of the magnetic core. The optimized design results are given in Table IX.

C. Design of 5P-SPT

A 5P-SPT of the same rating is also designed and optimized to facilitate the comparison. The 5P-SPT consists of five SPTs.

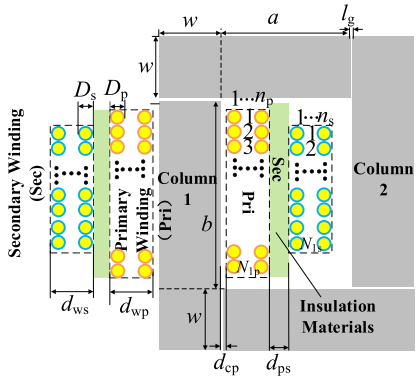

Fig. 28. Structure of the 5P-SPT.

TABLE X
OPTIMIZED DESIGN OF A SINGLE TRANSFORMER IN THE 5P-SPT

Parameters	Value	Parameters	Value
a (mm)	56	V_{tr} (dm^3)	5.34×5
b (mm)	105	S (cm^2)	1634.79×5
w (mm)	55	P_{core} (W)	47.38×5
h	1	$P_{winding}$ (W)	49.6×5
N_p	12	P_{tot} (W)	97.02×5
k_p	1130	γ (kW/dm^3)	7.48
k_s	1565	S_{heat} (cm^2/W)	16.85
n_p	1		
n_s	1		

TABLE XI
OPTIMIZED DESIGN OF THE DOWN-SCALED 5P-MIT PROTOTYPE

Parameters	Value	Parameters	Value
l (mm)	30	V_{tr} (dm^3)	2.84
b (mm)	45	S (cm^2)	1762.29
N_p	9	P_{core} (W)	17.22
k_p	290	$P_{winding}$ (W)	3.23
k_s	300	P_{tot} (W)	20.45
n_p	1	γ (kW/dm^3)	1.13
n_s	1	S_{heat} (cm^2/W)	86.18

The structure of one single transformer is depicted in Fig. 28. The optimized design results are given in Table X.

D. Design of the Down-Scaled 5P-MIT Prototype

To valid the design of the proposed 5P-MIT and the functionality of the 5P-LLC resonant converter, a down-scaled 5P-MIT is designed, optimized, and constructed. The optimized design results are given in Table XI.

REFERENCES

[1] Y. Gu, Z. Lu, L. Hang, Z. Qian, and G. Huang, "Three-level LLC series resonant DC/DC converter," *IEEE Trans. Power Electron.*, vol. 20, no. 4, pp. 781–789, Jul. 2005.

[2] S. De Simone, C. Adragna, C. Spini, and G. Gattavari, "Design-oriented steady-state analysis of LLC resonant converters based on FHA," in *Proc. Int. Symp. Power Electron., Elect. Drives Autom. Motion*, 2006, pp. 200–207.

[3] T. Zhao *et al.*, "Analysis and suppression of resonant current envelope ripple of LLC converter in cascaded modular PV solid-state transformer," *IEEE J. Emerg. Sel. Topics Power Electron.*, vol. 9, no. 3, pp. 3744–3757, Jun. 2021.

[4] M. Wang *et al.*, "Module power balance control strategy for three-phase cascaded H-Bridge PV inverter under unbalanced grid voltage condition," *IEEE J. Emerg. Sel. Topics Power Electron.*, vol. 9, no. 5, pp. 5657–5671, Oct. 2021.
[5] K. Zhang, Y. Chen, M. Zhu, Z. Wang, and H. Liu, "An input independent output series energy-stored quasi-Z source LLC converter for application to DC photovoltaic system," in *Proc. IEEE 12th Energy Convers. Congr. Expo. Asia*, 2021, pp. 2157–2162.
[6] H. Wang and Z. Li, "A PWM LLC type resonant converter adapted to wide output range in PEV charging applications," *IEEE Trans. Power Electron.*, vol. 33, no. 5, pp. 3791–3801, May 2018.
[7] Z. Li, T. Wu, G. Zhang, and R. Yang, "Hybrid modulation method combining variable frequency and double phase-shift for a 10 kW LLC resonant converter," *IET Power Electron.*, vol. 11, no. 13, pp. 2161–2169, Jul. 2018.
[8] G. Ortiz, M. G. Leibl, J. E. Huber, and J. W. Kolar, "Design and experimental testing of a resonant DC–DC converter for solid-state transformers," *IEEE Trans. Power Electron.*, vol. 32, no. 10, pp. 7534–7542, Oct. 2017.
[9] S. Zhao, Q. Li, F. C. Lee, and B. Li, "High-frequency transformer design for modular power conversion from medium-voltage AC to 400 VDC," *IEEE Trans. Power Electron.*, vol. 33, no. 9, pp. 7545–7557, Sep. 2018.
[10] Y. Yu, G. Konstantinou, B. Hredzak, and V. G. Agelidis, "Operation of cascaded H-bridge multilevel converters for large-scale photovoltaic power plants under bridge failures," *IEEE Trans. Power Electron.*, vol. 62, no. 11, pp. 7228–7236, Nov. 2015.
[11] D. Rothmund, T. Guillod, D. Bortis, and J. W. Kolar, "99% efficient 10 kV SiC-based 7 kV/400 V DC transformer for future data centers," *IEEE J. Emerg. Sel. Topics Power Electron.*, vol. 7, no. 2, pp. 753–767, Jun. 2019.
[12] T. Guillod, R. Färber, F. Krismer, C. M. Franck, and J. W. Kolar, "Computation and analysis of dielectric losses in MV power electronic converter insulation," in *Proc. IEEE Energy Convers. Congr. Expo.*, Sep. 2016, pp. 1–8.
[13] Y. Nakakohara, H. Otake, T. M. Evans, T. Yoshida, M. Tsuruya, and K. Nakahara, "Three-phase LLC series resonant DC/DC converter using SiC mosfets to realize high-voltage and high-frequency operation," *IEEE Trans. Ind. Electron.*, vol. 63, no. 4, pp. 2103–2110, Apr. 2016.
[14] S. A. Arshadi, M. Ordonez, W. Eberle, M. A. Saket, M. Craciun, and C. Botting, "Unbalanced three-phase LLC resonant converters: Analysis and trigonometric current balancing," *IEEE Trans. Power Electron.*, vol. 34, no. 3, pp. 2025–2038, Mar. 2019.
[15] S. A. Arshadi, M. Ordonez, W. Eberle, M. Craciun, and C. Botting, "Three-phase LLC battery charger: Wide regulation and improved light-load operation," *IEEE Trans. Power Electron.*, vol. 36, no. 2, pp. 1519–1531, Feb. 2021.
[16] T. Qian and B. Lehman, "Coupled input-series and output-parallel dual interleaved flyback converter for high input voltage application," *IEEE Trans. Power Electron.*, vol. 23, no. 1, pp. 88–95, Jan. 2008.
[17] Q. Li and P. Wolfs, "A current fed two-inductance boost converter with an integrated magnetic structure and passive lossless snubbers for photovoltaic module integrated converter applications," *IEEE Trans. Power Electron.*, vol. 22, no. 1, pp. 309–321, Jan. 2007.
[18] C. W. T. McLyman, *Transformer and Inductance Design Handbook*, 4th ed. Boca Raton, FL, USA: CRC Press, 2011.
[19] M. Mogorovic and D. Dujic, "100 kW, 10 kHz medium-frequency transformer design optimization and experimental verification," *IEEE Trans. Power Electron.*, vol. 34, no. 2, pp. 1696–1708, Feb. 2019.
[20] J. Jung, "Bifilar winding of a center-tapped transformer including integrated resonant inductance for LLC resonant converters," *IEEE Trans. Power Electron.*, vol. 28, no. 2, pp. 615–620, Feb. 2013.
[21] Bo Yang, R. Chen, and F. C. Lee, "Integrated magnetic for LLC resonant converter," in *Proc. 17th Annu. IEEE Appl. Power Electron. Conf. Expo.*, 2002, vol. 1, pp. 346–351.
[22] W. Martinez *et al.*, "Three-phase LLC resonant converter with integrated magnetics," in *Proc. IEEE Energy Convers. Congr. Expo.*, Sep. 2016, pp. 1–8.
[23] M. Noah *et al.*, "A current sharing method utilizing single balancing transformer for a multiphase LLC resonant converter with integrated magnetics," *IEEE J. Emerg. Sel. Topics Power Electron.*, vol. 6, no. 2, pp. 977–992, Jun. 2018.
[24] M. Noah, K. Umetani, J. Imaoka, and M. Yamamoto, "Lagrangian dynamics model and practical implementation of an integrated transformer in multi-phase LLC resonant converter," *IET Power Electron.*, vol. 11, no. 2, pp. 339–347, 2018.
[25] M. Noah, K. Umetani, S. Endo, H. Ishibashi, J. Imaoka, and M. Yamamoto, "A lagrangian dynamics model of integrated transformer incorporated in a multi-phase LLC resonant converter," in *Proc. IEEE Energy Convers. Congr. Expo.*, 2017, pp. 3781–3787.
[26] M. Noah *et al.*, "Magnetic design and experimental evaluation of a commercially available single integrated transformer in three-phase LLC resonant converter," *IEEE Trans. Ind. Appl.*, vol. 54, no. 6, pp. 6190–6204, Nov./Dec. 2018.
[27] X. Yu, J. Su, J. Lai, and S. Guo, "Analytical optimization of nonsaturated thermally limited high-frequency transformer/inductor design considering discreteness of design variables," *IEEE Trans. Power Electron.*, vol. 35, no. 6, pp. 6231–6250, Jun. 2020.
[28] W. G. Hurley and W. H. Wolfle. *Transformers and Inductors For Power Electronics*. Hoboken, NJ, USA: Wiley, 2013.
[29] X. Cao, W. Chen, G. Ning, G. Qiao, and C. Wang, "Optimization design of High-power High-frequency transformer based on Multi-objective genetic algorithm," *Proc. Chin. Soc. Elect. Eng.*, vol. 38, no. 6, pp. 1348–1355, Mar. 2018.
[30] M. Leibl, G. Ortiz, and J. W. Kolar, "Design and experimental analysis of a medium-frequency transformer for solid-state transformer applications," *IEEE J. Emerg. Sel. Topics Power Electron.*, vol. 5, no. 1, pp. 110–123, Mar. 2017.
[31] M. A. Bahmani, T. Thiringer, and M. Kharezy, "Design methodology and optimization of a medium-frequency transformer for high-power DC–DC applications," *IEEE Trans. Ind. Appl.*, vol. 52, no. 5, pp. 4225–4233, Sep./Oct. 2016.
[32] M. S. Rylko, B. J. Lyons, J. G. Hayes, and M. G. Egan, "Revised magnetics performance factors and experimental comparison of high-flux materials for high-current DC–DC inductors," *IEEE Trans. Power Electron.*, vol. 26, no. 8, pp. 2112–2126, Aug. 2011.
[33] W. Shen, F. Wang, D. Boroyevich, and C. W. Tipton, "Loss characterization and calculation of nanocrystalline cores for high-frequency magnetics applications," *IEEE Trans. Power Electron.*, vol. 23, no. 1, pp. 475–484, Jan. 2008.
[34] Magnetics, "2020 Magnetics powder core catalog [EB/OL]," [Online]. Available: https://www.mag-inc.com/Design/Technical-Documents/Powder-Core-Documents?lang=en-US
[35] K. Deb, A. Pratap, S. Agarwal, and T. Meyarivan, "A fast and elitist multiobjective genetic algorithm: NSGA-II," *IEEE Trans. Evol Comput.*, vol. 6, no. 2, pp. 182–197, Apr. 2002.

Jianing Wang (Member, IEEE) received the M.S. degree in power electronics from the Power Electronics and Renewable Energy Center, Xi'an Jiaotong University, Xi'an, China, in 2010, and the Ph.D. degree from the Electrical Power Processing Group (EPP), Faculty of Electrical Engineering, Delft University of Technology, Delft, The Netherlands, in 2014.

In 2014, he joined Hefei University of Technology as an Associate Professor. He has successfully leaded multiple projects as PI. His research interests include high power density power converters, power module packaging, automatic design of power electronics, etc.

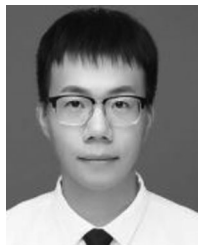

Jiawen Hu received the B.S. degree from Faculty of Electrical Engineering and Computer Science, Ningbo University, Ningbo, China, in 2019. He is currently working toward the M.S. degree with the School of Electrical Engineering and Automation, Hefei University of Technology, Hefei, China.

His research interests include high efficiency high power dc/dc converters.

Wei Pei received the B.S. degree from the School of Electrical Information Engineering, Jiangsu University, Zhenjiang, China, in 2020. He is currently working toward the M.S. degree from the School of Electrical Engineering and Automation, Hefei University of Technology, Hefei, China.

His research interests include high efficiency high power dc/dc converters.

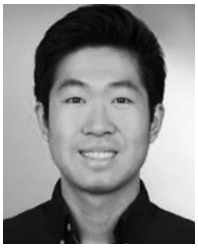

Zhiqing Yang (Member, IEEE) received the B.S. degree from Southwest Jiaotong University, Chengdu, China, in 2013, and the M.S. and Dr.-Ing. degrees from RWTH Aachen University, Aachen, Germany, in 2017 and 2021, respectively, all in electrical engineering.

From April 2016 to September 2016, he was a Research Intern with Advanced Technology R&D Center, Mitsubishi Electric, Amagasaki, Japan. Since January 2022, he joined the School of Electrical Engineering and Automation, Hefei University of Technology, as an Associate Professor. His research interests include modeling, control, and integration of power electronic systems.

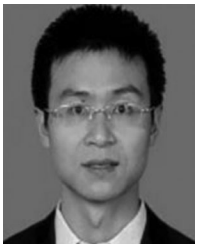

Jiacai Zhuang received the B.S. degree in measurement and control technology and instruments from the Nanjing University of Aeronautics and Astronautics, in 2007. He began to research power electronic devices and equipment, in 2007, and focus on photovoltaic power generation system research, in 2010. He currently works with Sungrow Power Supply Company, Ltd., mainly responsible for the pre research of new generation of new energy power generation systems.

Xing Zhang (Senior Member, IEEE) received the B.S. degree in automation, the M.S. degree in automation, and the Ph.D. degree in electrical engineering from the Hefei University of Technology (HFUT), Hefei, China, in 1984, 1990, and 2003, respectively.

In 1984, he joined the Teaching Faculty of the School of Electrical Engineering and Automation, HFUT, where he is currently a Professor and also with Photovoltaic Engineering Research Center, Ministry of Education, China. He is an Associate Editor for the IEEE JOURNAL OF EMERGING AND SELECTED TOPICS IN POWER ELECTRONICS. He is cooperating with the Sungrow Power Supply Company Ltd., Hefei, China, for a long time in the area of power electronics. His main research interests include photovoltaic generation technologies, wind power generation technologies, and distributed generation system.